Talanta 298 (2026) 129068

Contents lists available at ScienceDirect

Talanta

journal homepage: www.elsevier.com/locate/talanta

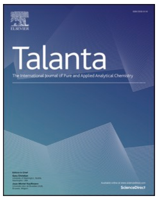

Dynamic *in vivo* imaging of microplastic-induced hepatic injury via enzyme-activated far-red fluorescent probe

Lanyun Zhang [a], Mo Ma [a,c], Chen Zhao [a], Jingkang Li [a], Siqi Zhang [a], Pinyi Ma [a,*], Bo Zhang [b,**], Daqian Song [a,***]

[a] *College of Chemistry, Jilin Province Research Center for Engineering and Technology of Spectral Analytical Instruments, Jilin University, Qianjin Street 2699, Changchun, 130012, China*
[b] *International Center of Future Science, Jilin University, Qianjin Street 2699, Changchun, 130012, China*
[c] *School of Pharmacy, Jilin University, Qianjin Street 2699, Changchun, 130012, China*

ARTICLE INFO

Keywords:
Chymotrypsin
Microplastic toxicity
Far-red probe
Liver injury imaging
Environmental bioaccumulation

ABSTRACT

Microplastic pollution, particularly from polystyrene (PS), poses increasing risks to human health due to its persistence in the environment, tendency to bioaccumulate, and ability to induce oxidative stress and hepatic injury. However, tools for dynamic imaging that elucidate the mechanistic link between microplastic exposure and liver toxicity remain lacking. Herein, we report a far-red fluorescent probe (emission maximum at 674 nm), DDAO-CT, derived from the hydroxyl-substituted red-emitting fluorophore DDAO (9,9-dimethylacridin-2(9H)-one derivative), designed for *in vivo* visualization of chymotrypsin activity, a key enzyme marker known to be upregulated during microplastic-induced liver damage. DDAO-CT is constructed by conjugating a 4-bromobutyryl recognition group to the red-emissive fluorophore DDAO, which quenches fluorescence by disrupting intramolecular charge transfer (ICT). Upon enzymatic hydrolysis by chymotrypsin, the ICT pathway is restored, resulting in a 14-fold enhancement in fluorescence at 674 nm with a detection limit of 3.5 ng/mL. The probe had high selectivity, low cytotoxicity, and excellent responsiveness to enzyme activity both *in vitro* and in PS-exposed hepatocytes. Notably, *in vivo* imaging in mouse models revealed dose-dependent fluorescence signals in the liver, which correlated closely with histopathological damage and elevated serum markers of liver injury. These results show that chymotrypsin activation is a downstream event of PS bioaccumulation, establishing DDAO-CT as an effective tool for visualizing pollutant-induced hepatic dysfunction. This study presents a novel chemical biology platform for noninvasive assessment of environmental hepatotoxins and offers mechanistic insights into microplastic-induced liver injury at the enzymatic level.

1. Introduction

The widespread use of plastic products has led to a global microplastic pollution crisis [1–5]. Among various types, polystyrene (PS) microplastics are particularly persistent in the environment and prone to bioaccumulation [6–10]. Their surfaces can adsorb heavy metals and persistent organic pollutants, resulting in synergistic toxicity through the food chain, from aquatic organisms and crops to humans [11–17]. As the primary organ for metabolism and detoxification, the liver is especially vulnerable to microplastic-induced toxicity. Growing evidence suggests that PS microplastics can trigger a cascade of oxidative stress, inflammation, and ferroptosis in the liver, ultimately leading to hepatocellular necrosis, fibrosis, and metabolic dysfunction [18–21]. However, dynamic visualization strategies capable of monitoring the *in vivo* accumulation of PS microplastics and elucidating their hepatotoxic mechanisms remain lacking.

Chymotrypsin, a serine protease secreted primarily by the pancreas, cleaves peptide bonds at the carboxyl termini of aromatic amino acids [22–27]. Studies have demonstrated that exposure to PS microplastics causes hepatic pathology, in which chymotrypsin plays a protective role by suppressing inflammation and oxidative stress [18,28–32]. Given its critical role in counteracting liver injury, monitoring chymotrypsin

---

[*] Corresponding author.
[**] Corresponding author.
[***] Corresponding author.

E-mail addresses: mapinyi@jlu.edu.cn (P. Ma), bozhang2019@jlu.edu.cn (B. Zhang), songdq@jlu.edu.cn (D. Song).

https://doi.org/10.1016/j.talanta.2025.129068
Received 26 August 2025; Received in revised form 28 October 2025; Accepted 2 November 2025

activity could serve as a valuable biomarker for assessing the body's compensatory response to microplastic-induced hepatotoxicity [33–41]. However, currently available fluorescent probes targeting chymotrypsin suffer from significant drawbacks, including complex synthesis, low yields, high background interference, short emission wavelengths, and poor tissue penetration [33–35,37]. These drawbacks limit the development of tools capable of real-time, specific imaging of endogenous chymotrypsin activity *in vivo*.

To address these challenges, we developed 6,8-dichloro-9,9-dimethyl-7-oxo-7,9-dihydroacridin-2-yl-4-bromobutanoate (DDAO-CT), a far-red fluorescent probe, for specific imaging of chymotrypsin activity in models of PS-exposed liver injury. This probe was developed based on 1,3-dichloro-7-hydroxy-9,9-dimethylacridin-2(9H)-one (DDAO), red-emitting acridone fluorophore, a red-emissive fluorophore with excellent optical properties, and synthesized via a simple esterification reaction. Recognition groups were attached to disrupt the D-π-A conjugated structure, leading to fluorescence quenching. Upon hydrolysis by chymotrypsin, an acyl-enzyme complex is formed, leading to an intramolecular charge transfer (ICT) effect that restores fluorescence, resulting in a strong far-red fluorescent signal at 674 nm. This design can effectively overcome the limitations of short-wavelength emission and enhance penetration capability and detection sensitivity. Strong fluorescent signals were observed in liver cancer cells exposed to PS, confirming a link between microplastic exposure and chymotrypsin activation. *In vivo* experiments further demonstrated that the probe could localize the lesions of drug-induced liver injury in mice and, through gradient concentration, revealed the dose-response of microplastics *in vivo*. To our knowledge, this study is the first to achieve dynamic *in vivo* visualization of microplastic-induced hepatotoxicity. The three-level validation, from *in vitro* studies to cell models to *in vivo* experiments, provides important evidence for understanding the mechanism by which microplastics induce liver damage through bioaccumulation and amplification effects.

2. Experimental section

2.1. Materials and instruments

Detailed information on all chemicals, reagents, and instrumentation is available in the Supplementary Materials.

2.2. Synthesis of the probe

Fig. 1 shows the synthetic route for DDAO-CT (6,8-Dichloro-9,9-dimethyl-7-oxo-7,9-dihydroacridin-2-yl-4-bromobutanoate).

4-Bromobutyryl chloride was prepared by reacting 500 μL of 4-bromobutyric acid with 2 mL of sulfuryl chloride in a 25 mL round-bottom flask, using 1–2 drops of DMF as a catalyst. The reaction was carried out for 2 h, after which excess reagents were removed under reduced pressure. The resulting product was used directly in the subsequent steps without purification.

To synthesize 1,3-dichloro-7-hydroxy-9,9-dimethylacridin-2(9H)-one (DDAO), Compound 1 (1.52 g, 10 mmol) and Compound 2 (2.1 g, 10 mmol) were dissolved in a 1:1 (v/v) mixture of THF and water (20 mL) and the mixture was sonicated. After cooling the mixture in an ice bath, 8 mL of 2 M NaOH was added dropwise. The reaction mixture was thereafter stirred at low temperature for 1.5 h. The mixture was then extracted with ethyl acetate, and the aqueous phase was back-extracted. The combined organic phases were washed with 1 M $Na_2S_2O_4$, dried over anhydrous Na_2SO_4, and concentrated *in vacuo*. The resulting crude product was treated with 2 M HCl (40 mL) in methanol and refluxed at 100 °C for 2 h. After cooling, the mixture was extracted with ethyl acetate, washed with $NaIO_4$, and recrystallized from ethanol, which yielded DDAO as a dark-red solid (649 mg, 42 % yield). ^1H NMR (600 MHz, DMSO) δ 11.12 (s, 1H), 7.77 (s, 1H), 7.50 (d, $J = 8.6$ Hz, 1H), 7.15 (d, $J = 2.1$ Hz, 1H), 6.93 (ddd, $J = 8.5, 2.4, 0.7$ Hz, 1H), 1.78 (s, 6H). ^{13}C NMR (151 MHz, DMSO) δ 172.63, 163.39, 154.13, 146.08, 141.65, 141.43, 139.76, 135.01, 134.74, 132.92, 116.54, 114.68, 39.26, 26.74 (Figs. S1–S2). HR-MS (*m/z*): $[M+H]^+$ calcd for $C_{15}H_{12}Cl_2NO_2^+$: 308.0240; found: 308.0240 (Fig. S3).

For the synthesis of DDAO-CT, DDAO (150 mg, 0.5 mmol) was dissolved in 15 mL of dichloromethane, followed by the addition of 150 μL of 4-bromobutyryl chloride and 80 μL of triethylamine. The mixture was stirred in an ice bath for 2 h. Upon completion of the reaction (as monitored by TLC), the crude product was purified by column chromatography using petroleum ether/ethyl acetate (10:1) as the eluent, yielding DDAO-CT as a yellow solid (120 mg, 53 % yield). ^1H NMR (600 MHz, $CDCl_3$) δ 7.67 (d, $J = 8.5$ Hz, 1H), 7.64 (s, 1H), 7.25 (d, $J = 2.5$ Hz, 1H), 7.15 (dd, $J = 8.6, 2.4$ Hz, 1H), 3.56 (t, $J = 6.3$ Hz, 2H), 2.83 (t, $J = 7.2$ Hz, 2H), 2.35–2.27 (m, 2H), 1.89 (s, 6H). ^{13}C NMR (150 MHz, $CDCl_3$) δ 173.17, 170.60, 153.15, 149.89, 140.29, 139.49, 139.43, 138.60, 137.43, 135.63, 133.10, 121.40, 119.75, 39.10, 32.58, 32.37, 27.41, 26.68. (Figs. S4–S5). HR-MS (*m/z*): $[M+H]^+$ calcd for $C_{19}H_{17}BrCl_2NO_3^+$: 455.9763; found: 455.9763 (Fig. S6).

2.3. Spectral analysis

A 1 mM stock solution of DDAO-CT was prepared by dissolving 1 mg of the probe in 2.2 mL of anhydrous DMSO. Chymotrypsin was freshly diluted in ultrapure water to the desired concentrations. For fluorescence measurements, 10 μL of probe solution and PBS buffer (10 mM, pH 7.4) were mixed with varying concentrations of chymotrypsin in a 1.5 mL microtube. The final reaction volume was adjusted to 1 mL (containing 1 % DMSO). Samples were incubated at 37 °C in a shaker for 40 min before spectral analysis. Fluorescence spectra were recorded at an excitation wavelength of 600 nm, with both excitation and emission slit widths set to 5 nm. The photomultiplier tube (PMT) voltage was maintained at 700 V.

2.4. Cell culture and imaging

HepG2 cells were cultured in DMEM supplemented with 10 % fetal bovine serum and 1 % penicillin–streptomycin under standard conditions (37 °C, 5 % CO_2). After passaging and seeding, cells were divided into four groups according to the treatment received: (1) Control group; (2) 50 μg/mL PS suspension for 12 h; (3) PS (50 μg/mL, 12 h) followed

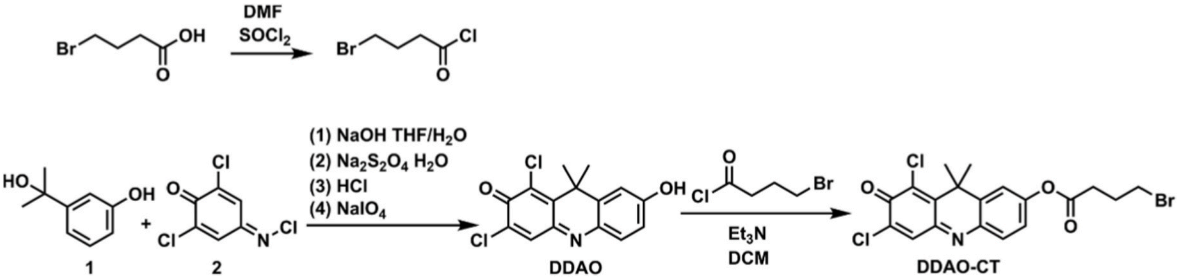

Fig. 1. Synthetic route of probe DDAO-CT.

by 1 mM PMSF (phenylmethylsulfonyl fluoride) (12 h); and (4) PS (50 μg/mL, 12 h) followed by 2 mM AEBSF (4-(2-aminoethyl)benzenesulfonyl fluoride hydrochloride) (12 h). For concentration-dependent studies, cells were treated with PS at 10, 30, 50, and 100 μg/mL for 12 h. For time-course studies, cells were treated with 50 μg/mL PS for 6, 12, 18, and 24 h. After treatment, all groups were washed with PBS and incubated with 10 μM DDAO-CT for 1 h in the dark before imaging.

2.5. *Establishment of mouse models*

In microplastic-induced liver injury experiments, BALB/c mice (purchased from Beijing Sibeifu Biotechnology Co., Ltd.) were randomly divided into a normal control group and a concentration-gradient exposure group. Mice in the exposure group were orally administered polystyrene (PS) microplastic suspensions at doses of 1 mg/kg/day, 20 mg/kg/day, and 50 mg/kg/day for 28 days. All animal procedures were approved by the Animal Ethics Committee of Jilin University (Approval No. SY202409007).

3. Results and discussion

3.1. *Probe design strategy*

To achieve specific detection of chymotrypsin, a far-red fluorescent probe, DDAO-CT, was rationally designed and synthesized. The probe comprises two key components: the fluorophore DDAO and the enzyme recognition moiety 4-bromobutyryl ester. The 4-bromobutyryl group is conjugated to the hydroxyl position of DDAO, which reduces the electron-donating ability of the hydroxyl group and disrupts the ICT process, effectively quenching the fluorescence of DDAO. Upon enzymatic cleavage of the ester bond by chymotrypsin, the D-π-A structure of DDAO is restored, resulting in a fluorescence "turn-on" response. This mechanism enables selective activation of the fluorescent signal in the presence of chymotrypsin. Fig. 2 illustrates the fluorescence activation mechanism of the DDAO-CT probe.

3.2. *Reaction mechanism*

Theoretical calculations revealed that the HOMO–LUMO bandgap of DDAO-CT (2.93 eV) is significantly larger compared to that of the parent DDAO fluorophore (2.34 eV), which explains the observed blue shift in the UV–Vis absorption spectra upon structural modification (Fig. 3A). More importantly, the introduction of the 4-bromobutyryl group disrupted the intrinsic intramolecular charge transfer (ICT) process of DDAO, leading to its fluorescence quenching as the primary cause (Fig. 4A). Upon chymotrypsin-catalyzed hydrolysis, the recognition group is cleaved, leading to the restoration of the ICT pathway and the reactivation of the far-red fluorescence. Molecular docking simulations using AutoDock Vina (PDB ID: 2P8O) revealed a stable binding between DDAO-CT and chymotrypsin with a binding energy of −6.8 kcal/mol. Detailed interaction analysis (Fig. 3B) indicated that the ester carbonyl oxygen forms hydrogen bonds with LYS (Lysine) residues in chain C, while the central nitrogen atom interacts with GLY (Glycsine) residues. Additionally, the aromatic ring of DDAO engages in π–π stacking with TRP (Tryptophan) residues and forms van der Waals interactions with HIS (Histidine) and MET (Methionine) residues. Alkyl–π interactions with ILE (Isoleucine) residues further contribute to the stabilization of the complex. These non-covalent interactions underpin the specificity of DDAO-CT toward chymotrypsin.

3.3. *Spectral response to chymotrypsin*

The responsiveness of DDAO-CT to chymotrypsin was evaluated by monitoring spectral changes before and after enzymatic treatment. UV–Vis spectroscopy revealed that a red shift in the probe's absorption peak from 445 nm to 635 nm following incubation with chymotrypsin, indicating the release of the DDAO fluorophore (Fig. 4A). Correspondingly, fluorescence measurements showed a weak emission at 660 nm in the unreacted state, which shifted to a strong emission at 674 nm after enzymatic cleavage (Fig. 4B). These results confirm the efficient activation of the probe and restoration of the fluorescence, consistent with the intrinsic emission characteristics of DDAO.

3.4. *Optimization of reaction conditions*

To determine the optimal enzymatic reaction conditions for DDAO-CT, both pH and temperature were systematically investigated. The probe exhibited weak background fluorescence under physiological conditions, while the overall fluorescence response increased across the pH range of 6.0–8.5 upon activation by chymotrypsin. The maximum fluorescence enhancement was observed at pH 7.4, indicating that the catalytic efficiency is optimal under neutral conditions (Fig. S7). Temperature-dependent experiments demonstrated that fluorescence signals remained relatively stable between 25 and 42 °C, with at 37 °C (Fig. S8). These results confirm that pH 7.4 and 37 °C are the optimal conditions for efficient interaction between DDAO-CT and chymotrypsin.

3.5. *Time-dependent response and photostability*

Time-course fluorescence experiments revealed that the fluorescence of DDAO-CT rapidly increased during the first 40 min, followed by a slower rise until reaching a plateau at 70 min (Fig. S9). Therefore, a 70-min incubation time was selected for subsequent assays to ensure complete enzymatic reaction. Photostability was evaluated under continuous excitation at 600 nm. The fluorescence intensity of both the free probe and enzyme-bound robe remained stable for up to 60 min of illumination, which is indicative of excellent photostability (Fig. S10). These properties support the suitability of the probe for real-time fluorescence imaging in biologically relevant conditions.

3.6. *Quantitative detection and sensitivity*

The fluorescence response of DDAO-CT to increasing concentrations of chymotrypsin (0–4000 ng/mL) was quantitatively evaluated under the optimal conditions (37 °C, pH 7.4, and 70-min incubation time). As shown in Fig. 4C, fluorescence intensity increased proportionally with enzyme concentration, reaching a 14-fold enhancement at equilibrium.

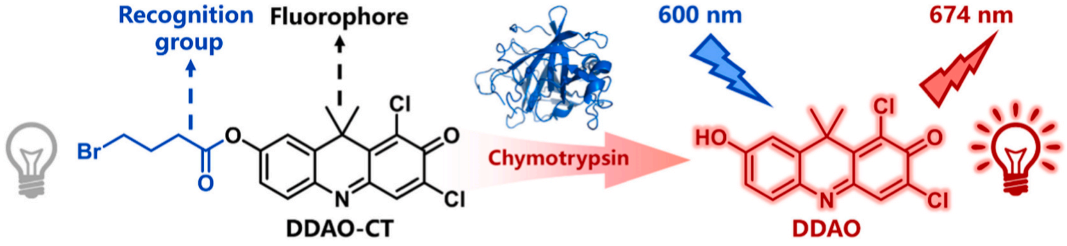

Fig. 2. Schematic illustration of the chymotrypsin-triggered fluorescence activation mechanism of the DDAO-CT probe.

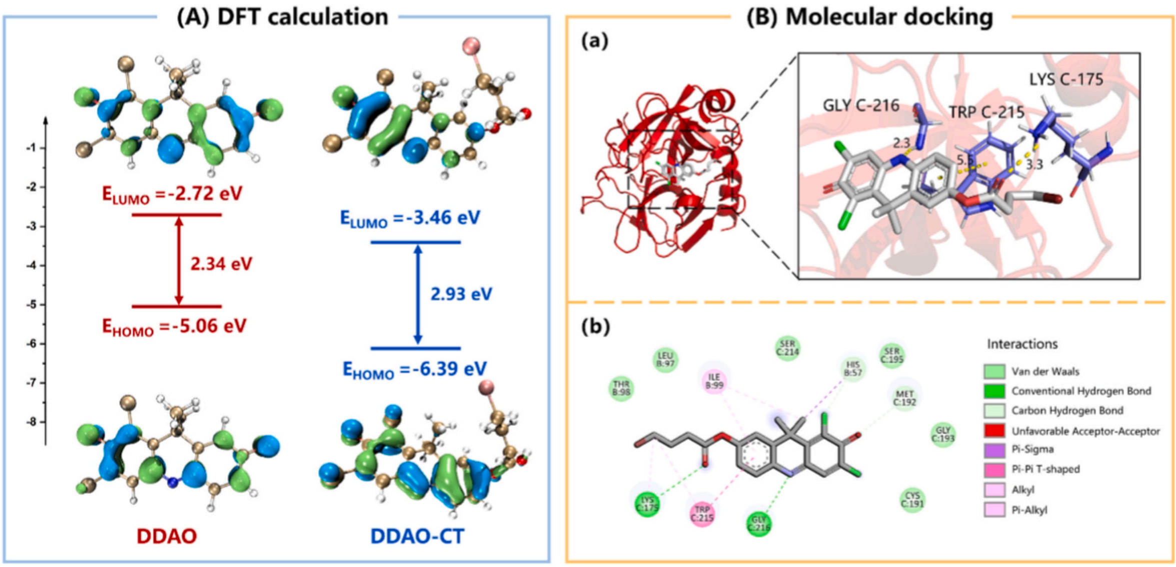

Fig. 3. (A) HOMO/LUMO energy levels of DDAO-CT and DDAO. (B) (a) Molecular docking of DDAO-CT with chymotrypsin visualized using PyMOL; and (b) interaction analysis of DDAO-CT and chymotrypsin using Discovery Studio.

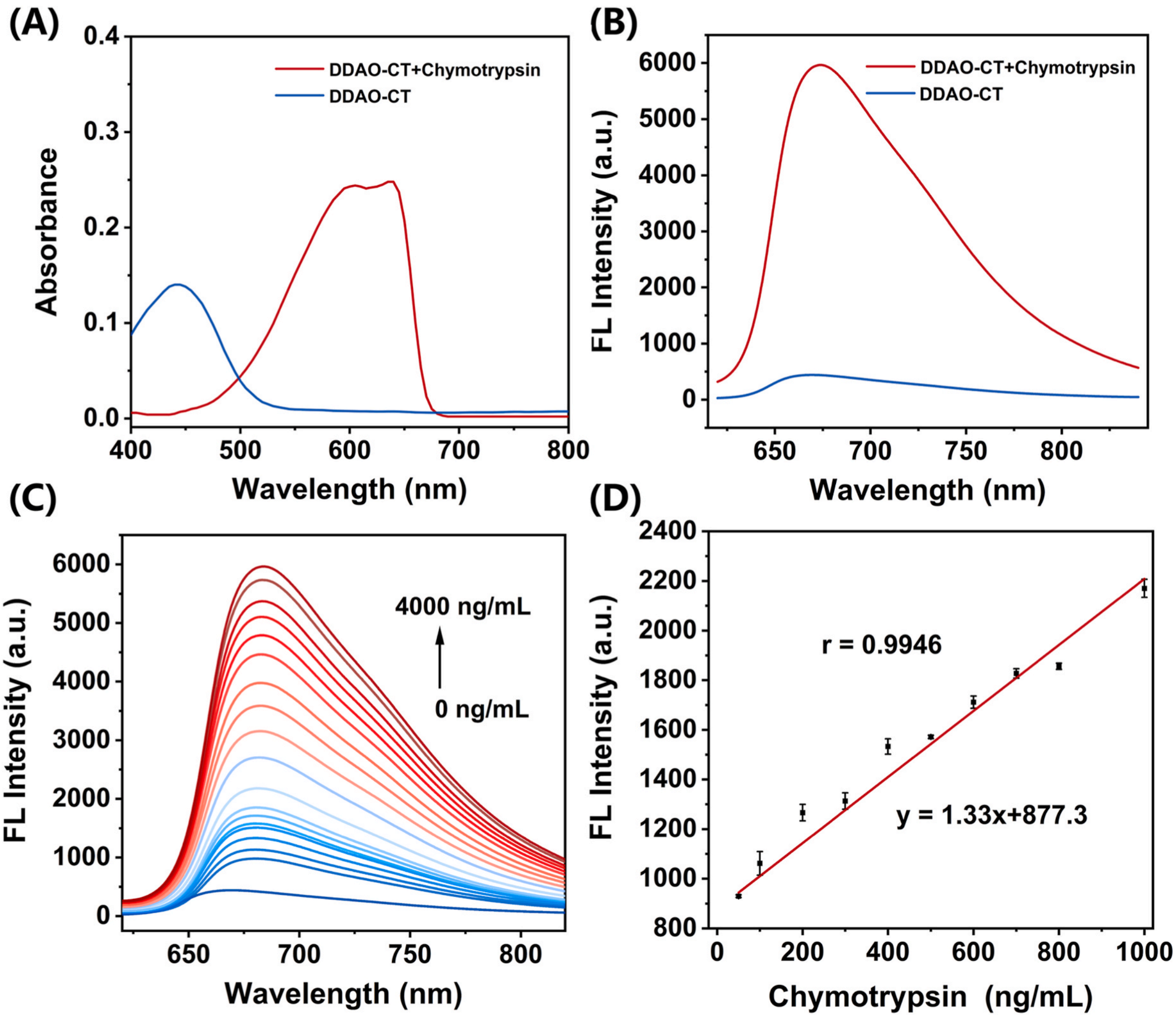

Fig. 4. (A) UV–Vis absorption spectra and (B) fluorescence emission spectra of DDAO-CT (10 μM) in the presence of chymotrypsin in PBS buffer. (C) Fluorescence intensity as a function of chymotrypsin concentration (0–4000 ng/mL). (D) Linear correlation between fluorescence intensity and chymotrypsin concentration (50–1000 ng/mL). (λ_{em} = 600 nm, λ_{ex} = 674 nm).

A linear correlation was observed in the range of 50–1000 ng/mL ($R^2 = 0.9946$) (Fig. 4D). The limit of detection (LOD), calculated using the 3σ/k method, was 3.5 ng/mL. Compared with existing chymotrypsin-specific fluorescent probes, DDAO-CT had superior performance, including lower detection limits and higher signal amplification (Table S1). These attributes highlight the potential of the probe for sensitive quantification of trace chymotrypsin activity in complex biological systems.

3.7. Selectivity toward chymotrypsin

The selectivity of DDAO-CT was assessed against 51 potential interferents, including various metal ions, amino acids, small biomolecules, and a panel of additional enzymes and proteins relevant to biological environments (Fig. S11). Upon identical incubation conditions, only chymotrypsin induced a significant fluorescence enhancement. These results demonstrate the high selectivity of DDAO-CT for chymotrypsin, and biologically abundant species had minimal interference.

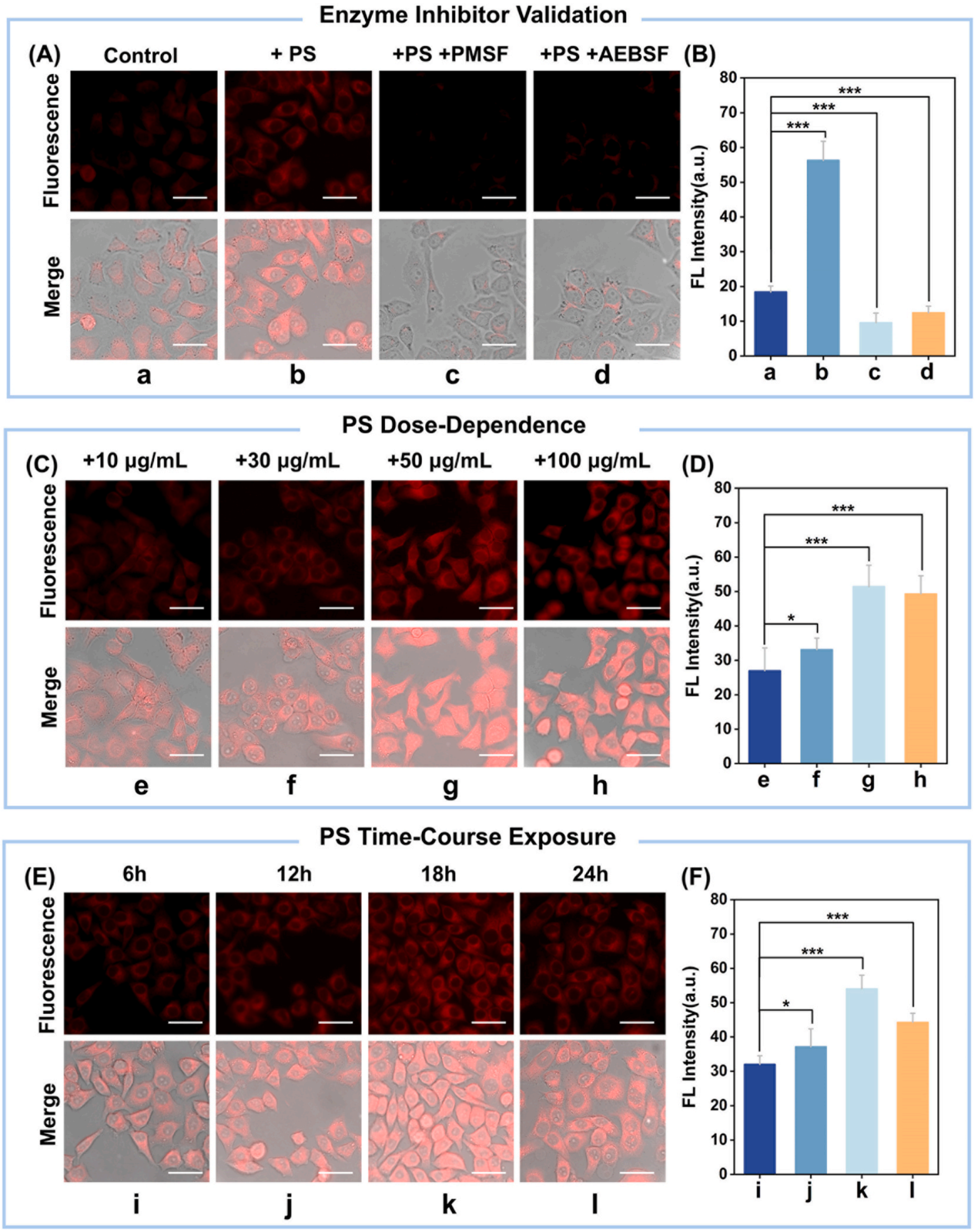

Fig. 5. (A) Fluorescence images of HepG2 cells in: (a) Control, (b) + PS, (c) + PS + PMSF, and (d) + PS + AEBSF groups. (B) Bar chart showing intracellular fluorescence intensity of cells in (A). (C) Fluorescence images of cells after 12 h treatment with PS at various concentrations: (e) 10, (f) 30, (g) 50, and (h) 100 μg/mL. (D) Bar chart showing intracellular fluorescence intensity of cells in (C). (E) Fluorescence images of cells after treatment with 50 μg/mL PS for (i) 6 h, (j) 12 h, (k) 18 h, and (l) 24 h. (F) Bar chart showing intracellular fluorescence intensity of cells in (E). The top rows in (A), (C), and (E) display fluorescence images, and the bottom rows show merged images. All scale bars: 40 μm.

3.8. *Cellular imaging of chymotrypsin activity*

3.8.1. *Cytotoxicity assessment*

The biocompatibility of DDAO-CT was evaluated in HepG2 cells using CCK-8 assays. Cell viability remained above 90 % at probe concentrations up to 50 μM, indicative of low cytotoxicity (Fig. S12). This result supports the suitability of DDAO-CT for live-cell fluorescence imaging applications.

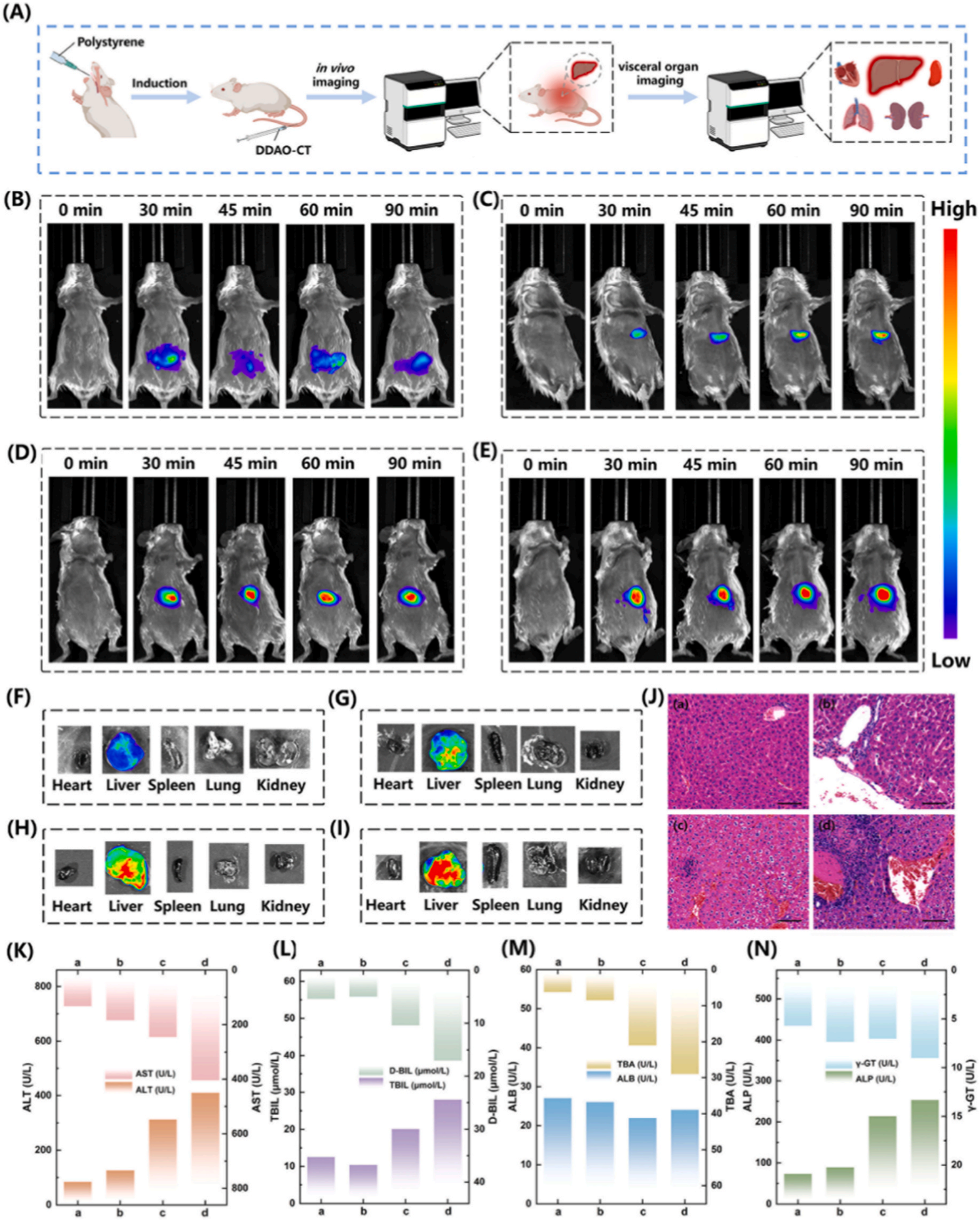

Fig. 6. (A) Schematic diagram of the experimental procedure. (B–E) Temporal fluorescence imaging showing dynamic changes in fluorescence signal in mice from each treatment group: (B) Normal mouse, (C) 1 mg/kg/day, (D) 20 mg/kg/day, and (E) 50 mg/kg/day. (F–I) Anatomical fluorescence imaging of major organs (heart, liver, spleen, lung, and kidney) from the corresponding groups: (F) Normal group, (G) 1 mg/kg/day, (H) 20 mg/kg/day, and (I) 50 mg/kg/day. (J) Liver sections from the corresponding groups: (a) Normal group, (b) 1 mg/kg/day, (c) 20 mg/kg/day, and (d) 50 mg/kg/day. Scale bar = 80 μm. (K–N) Liver function biochemical parameters: (K) ALT & AST (reference range: ALT, 28–132 U/L; AST, 59–247 U/L), (L) TBIL and D-BIL (reference range: TBIL, 1.7–15 μmol/L; D-BIL, 1.7–8.6 μmol/L), (M) ALB and TBA (reference range: ALB, 25–48 g/L; TBA, 1–10 μmol/L), (N) ALP and γ-GT (reference range: ALP, 62–209 U/L; γ-GT, 0–8 U/L). For all panels (K–N), a-d correspond to the normal, 1 mg/kg/day, 20 mg/kg/day, and 50 mg/kg/day groups, respectively.

3.8.2. *Inhibitor validation of endogenous enzyme activity*

Fluorescence imaging of HepG2 cells revealed weak background signals in the control group (Fig. 5A). Upon exposure to PS, intracellular red fluorescence significantly increased, an indication of chymotrypsin activation. In contrast, pretreatment with serine protease inhibitors, PMSF or AEBSF, markedly suppressed fluorescence recovery, demonstrating their irreversible inhibitory effects on chymotrypsin-like serine proteases by covalent modification of catalytic serine residues [42,43]. Quantitative analysis (Fig. 5B) confirmed that PS-induced enzyme activation was effectively inhibited, validating the ability of the probe to monitor endogenous chymotrypsin activity in live cells.

3.8.3. *Dose-dependent microplastic exposure*

To evaluate concentration-dependent effects, HepG2 cells were exposed to PS suspensions at various concentrations (10–100 μg/mL) for 12 h. Fluorescence imaging revealed a progressive increase in red fluorescence intensity with increasing PS concentration (Fig. 5C), consistent with elevated chymotrypsin activity. Quantitative fluorescence data (Fig. 5D) further confirmed a dose–dependent relationship. These results demonstrate that DDAO-CT can reliably visualize changes in enzyme activity induced by microplastic exposure.

3.8.4. *Time-dependent microplastic exposure*

Time-course studies using 50 μg/mL PS revealed dynamic changes in intracellular fluorescence (Fig. 5E). Signal intensity increased significantly between 6 and 18 h, reached its peak value at 18 h, and slightly declined at 24 h. Quantitative data (Fig. 5F) were also consistent with imaging results, further confirming that DDAO-CT can effectively track temporal fluctuations in chymotrypsin activity during microplastic exposure.

3.9. *In vivo fluorescence imaging and histopathological validation of PS-induced liver injury*

To investigate the applicability of DDAO-CT for dynamic imaging of microplastic-induced liver injury, BALB/c mice were exposed to polystyrene (PS) microplastics via oral gavage at doses of 1, 20, and 50 mg/kg/day for 28 days. Following intravenous injection of DDAO-CT, real-time fluorescence imaging was performed to monitor signal distribution in the abdominal region. As shown in Fig. 6B–E, fluorescence intensity in the abdominal region of mice in the microplastic-exposed groups progressively increased over time, with the strongest signal observed in the group receiving a dose of 50 mg/kg/day. The signal was spatially localized and temporally sustained, suggesting the activation of chymotrypsin in the abdominal region is dose-dependent.

Subsequent *ex vivo* fluorescence imaging of major organs (heart, liver, spleen, lung, and kidney) revealed that the fluorescence signal was predominantly localized in the liver (Fig. 6F–I). This confirms that the liver is the primary site of probe activation. The fluorescence intensity in the liver was positively correlated with microplastic dose, indicating the DDAO-CT's effectiveness in reporting enzyme activity associated with PS-induced hepatotoxicity.

Histopathological examination of liver sections further substantiated the imaging data. In the control group, hepatic lobular structures were intact, containing regularly arranged hepatocytes, and no signs of cellular degeneration or inflammatory infiltration were observed. In contrast, for mice exposed to 1 mg/kg/day PS, mild lymphocytic infiltration was observed in portal areas, and their lobular structure remained intact. At 20 mg/kg/day, focal hepatocellular necrosis became evident, as indicated by nuclear pyknosis and cytoplasmic vacuolization. The 50 mg/kg/day group (highest dose) exhibited widespread hepatocyte necrosis, nuclear fragmentation, and parenchymal disintegration, which are signs of severe liver damage (Fig. 6J). These histological changes aligned closely with the increasing fluorescence intensities, confirming the probe's ability to detect pathological severity.

To further validate hepatic injury, key serum biochemical indicators were quantified (Fig. 6K–N). Alanine aminotransferase (ALT) and aspartate aminotransferase (AST), classical markers of hepatocellular injury, were significantly elevated in the 20 and 50 mg/kg/day groups, surpassing normal reference ranges (28–132 U/L for ALT; 59–247 U/L for AST) [44,45]. Additionally, elevated levels of total bile acids (TBA) and direct bilirubin (D-BIL) were observed in high-dose groups, suggesting that cholestasis and hepatobiliary dysfunction occurred in these groups. These data are consistent with both fluorescence imaging and histopathological findings, providing multi-level validation of the probe's responsiveness.

To further validate hepatic injury, key serum biochemical indicators were quantified (Fig. 6K–N). Alanine aminotransferase (ALT) and aspartate aminotransferase (AST), established classical biomarkers of hepatocellular injury, were significantly elevated in the 20 and 50 mg/kg/day groups, with levels exceeding clinical reference ranges (28–132 U/L for ALT; 59–247 U/L for AST). This transaminase elevation aligns with the gold-standard diagnostic criteria for hepatocyte damage, demonstrating a dose-dependent hepatotoxic effect. Additionally, elevated levels of total bile acids (TBA) and direct bilirubin (D-BIL) were observed in high-dose groups, suggesting that cholestasis and hepatobiliary dysfunction occurred in these groups. These data are consistent with both fluorescence imaging and histopathological findings, providing multi-level validation of the probe's responsiveness.

Together, these results demonstrate that DDAO-CT is capable of sensitively imaging microplastic-induced hepatic injury *in vivo* in a dose-dependent manner. The observed correlation between microplastic dose, chymotrypsin activation, liver pathology, and biochemical dysfunction suggests that chymotrypsin activation is a key downstream event in the hepatotoxic cascade triggered by PS bioaccumulation.

4. Conclusion

This study presents the rational design and biological application of a far-red fluorescent probe, DDAO-CT, for dynamic imaging of chymotrypsin activity associated with PS microplastic-induced liver injury. The probe operates via an ICT modulation mechanism, in which a cleavable 4-bromobutyryl group quenches the native fluorescence of DDAO. Upon enzymatic hydrolysis by chymotrypsin, the ICT pathway is restored, allowing the probe to exhibit a strong fluorescence signal at 674 nm. DDAO-CT demonstrated high photostability, low background fluorescence, and excellent sensitivity, with a detection limit of 3.5 ng/mL, allowing for reliable quantification of trace chymotrypsin activity. *In vitro* and cellular experiments confirmed that DDAO-CT selectively responded to elevated chymotrypsin levels triggered by PS exposure. Fluorescence intensity positively correlated with both PS concentration and exposure duration. *In vivo* imaging demonstrated that the probe could visualize hepatic injury with high spatial resolution and distinguish the severity of liver damage caused by different microplastic exposure doses. These imaging results were further corroborated by histopathological examination and liver function biomarkers. Importantly, the study provides the first integrated evidence that PS bioaccumulation leads to chymotrypsin activation as a downstream molecular event in hepatotoxic progression. The DDAO-CT probe can serve as a robust and versatile tool for real-time tracking of enzyme activity in environmental toxicology models. It may be used to facilitate early-stage evaluation of liver injury caused by emerging environmental pollutants. Overall, this work expands the methodological toolkit for assessing microplastic toxicity and highlights the value of enzyme-activated probes in mechanistic toxicology.

CRediT authorship contribution statement

Lanyun Zhang: Writing – original draft, Validation, Investigation, Data curation, Conceptualization. **Mo Ma:** Investigation, Data curation. **Chen Zhao:** Investigation, Data curation. **Jingkang Li:** Investigation, Data curation. **Siqi Zhang:** Investigation, Data curation. **Pinyi Ma:** Writing – review & editing, Software, Project administration, Data curation. **Bo Zhang:** Writing – review & editing, Funding acquisition. **Daqian Song:** Software, Resources, Project administration, Funding acquisition.

Declaration of competing interest

The authors declare that they have no known competing financial interests or personal relationships that could have appeared to influence the work reported in this paper.

Acknowledgments

This work was supported by the National Natural Science Foundation of China (22004046 and 22074052) and the Science and Technology Developing Foundation of Jilin Province of China (20250206038ZP).

Appendix A. Supplementary data

Supplementary data to this article can be found online at https://doi.org/10.1016/j.talanta.2025.129068.

Data availability

Data will be made available on request.

References

[1] M. Shen, G. Zeng, Y. Zhang, X. Wen, B. Song, W. Tang, Can biotechnology strategies effectively manage environmental (micro)plastics? Sci. Total Environ. 697 (2019) 134200.

[2] D. Menéndez, A. Álvarez, S. Acle, P. Peón, A. Ardura, E. Garcia-Vazquez, Microplastics across biomes in diadromous species. Insights from the critically endangered Anguilla anguilla, Environ. Pollut. 305 (2022) 119277.

[3] H. Zhang, Q. Sun, Y. Liu, Y. Deng, S. Liu, J. Nan, et al., Polyethylene microplastic pollution changes the electrical resistance and thermal conductivity of loess soil, J. Environ. Manag. 371 (2024) 123127.

[4] T.S. Galloway, M. Cole, C. Lewis, Interactions of microplastic debris throughout the marine ecosystem, Nat. Ecol. Evol. 1 (2017) 116.

[5] A. Fricano, F. Bianchi, P. Di Filippo, D. Pomata, C. Riccardi, G. Simonetti, et al., Determination of additives as markers of microplastic contamination in the environment, Talanta 285 (2025) 127344.

[6] T. Kim, K. Park, J. Hong, Understanding the hazards induced by microplastics in different environmental conditions, J. Hazard Mater. 424 (2022) 127630.

[7] K.H.D. Tang, R. Li, Z. Li, D. Wang, Health risk of human exposure to microplastics: a review, Environ. Chem. Lett. 22 (2024) 1155–1183.

[8] A. Nithin, A. Sundaramanickam, P. Iswarya, O.G. Babu, Hazard index of microplastics contamination in various fishes collected off Parangipettai, Southeast Coast of India, Chemosphere 307 (2022) 136037.

[9] B. Iqbal, X. Zhao, K.Y. Khan, Q. Javed, M. Nazar, I. Khan, et al., Microplastics meet invasive plants: unraveling the ecological hazards to agroecosystems, Sci. Total Environ. 906 (2024) 167756.

[10] Y. Liu, H. Shi, L. Chen, X. Teng, C. Xue, Z. Li, An overview of microplastics in oysters: analysis, hazards, and depuration, Food Chem. 422 (2023) 136153.

[11] J. Guo, N. Liu, Q. Xie, L. Zhu, F. Ge, Polystyrene microplastics facilitate the biotoxicity and biomagnification of ZnO nanoparticles in the food chain from algae to daphnia, Environ. Pollut. 324 (2023) 121181.

[12] S. Varshney, M.M. Hegstad-Pettersen, P. Siriyappagouder, P.A. Olsvik, Enhanced neurotoxic effect of PCB-153 when co-exposed with polystyrene nanoplastics in zebrafish larvae, Chemosphere 355 (2024) 141783.

[13] J. Hu, Y. Zhu, J. Zhang, Y. Xu, J. Wu, W. Zeng, et al., The potential toxicity of polystyrene nanoplastics to human trophoblasts in vitro, Environ. Pollut. 311 (2022) 119924.

[14] Y. Cheng, Z. Fan, J. Wu, L. Li, G. Cheng, J. Yan, et al., Combined exposure of polystyrene nanoplastics and silver nanoparticles exacerbating hepatotoxicity in zebrafish mediated by ferroptosis pathway through increased silver accumulation, J. Hazard Mater. 492 (2025) 138260.

[15] P.J. Isaac Chandran, S. Veerasingam, Laser direct Infrared Spectroscopy: a cutting-edge approach to microplastic detection in environmental samples, Talanta 284 (2025) 127284.

[16] V. Morgado, C. Palma, R.J.N. Bettencourt da Silva, Microplastics identification by infrared spectroscopy – evaluation of identification criteria and uncertainty by the Bootstrap method, Talanta 224 (2021) 121814.

[17] X.-X. Zhou, R. Liu, L.-T. Hao, J.-F. Liu, Identification of polystyrene nanoplastics using surface enhanced Raman spectroscopy, Talanta 221 (2021) 121552.

[18] K. Zhang, J. Yang, L. Chen, J. He, D. Qu, Z. Zhang, et al., Gut microbiota participates in polystyrene microplastics-induced hepatic injuries by modulating the gut–liver axis, ACS Nano 17 (2023) 15125–15145.

[19] J. Cui, J. Teng, P. Xiang, F. Liu, Z. Cao, J. Lu, et al., A potent fluorescent probe for HOCl with dual NIR emissions: achieving the early diagnosis of polystyrene microplastics-induced liver injury involved in ferroptosis, J. Hazard Mater. 492 (2025) 138087.

[20] W. Lin, F. Hu, F. Liu, L. Liao, L. Ling, L. Li, et al., Microcystin-LR and polystyrene microplastics jointly lead to hepatic histopathological damage and antioxidant dysfunction in male zebrafish, Environ. Pollut. 347 (2024) 123789.

[21] M. Jiang, X. Li, C. Cai, Y. Xu, P. Song, J. Yu, Combined toxicity of polystyrene microplastics and perfluorobutane sulfonate on mouse liver: impact on lipid metabolism and gut-liver axis disruption, Ecotoxicol. Environ. Saf. 292 (2025) 117904.

[22] S. Takai, D. Jin, Pathophysiological role of chymase-activated matrix Metalloproteinase-9, Biomedicines 10 (2022) 2499.

[23] S. Ahmad, C.M. Ferrario, Chymase inhibitors for the treatment of cardiac diseases: a patent review (2010–2018), Expert Opin. Ther. Pat. 28 (2018) 755–764.

[24] T. Kuramoto, D. Jin, K. Komeda, K. Taniguchi, F. Hirokawa, S. Takai, et al., Chymase as a novel therapeutic target in acute pancreatitis, Int. J. Mol. Sci. 22 (2021) 12313.

[25] G. Pejler, Novel Insight into the in vivo function of mast cell chymase: lessons from knockouts and inhibitors, J. Innate Immun. 12 (2020) 357–372.

[26] J.-j. Ruan, W.-f. Weng, J. Yan, Y.-x. Zhou, H. Chen, M.-j. Ren, et al., Coix lacryma-jobi chymotrypsin inhibitor displays antifungal activity, Pestic. Biochem. Physiol. 160 (2019) 49–57.

[27] C.S. Henriques de Jesus, A.M. Chiorcea-Paquim, M.M. Barsan, V.C. Diculescu, Electrochemical assay for 20S proteasome activity and inhibition with anti-cancer drugs, Talanta 199 (2019) 32–39.

[28] X. Qian, P. Jin, K. Fan, H. Pei, Z. He, R. Du, et al., Polystyrene microplastics exposure aggravates acute liver injury by promoting Kupffer cell pyroptosis, Int. Immunopharmacol. 126 (2024) 111307.

[29] J. Liu, L. Zhang, F. Xu, S. Meng, H. Li, Y. Song, Polystyrene microplastics postpone APAP-induced liver injury through impeding macrophage polarization, Toxics 10 (2022) 792.

[30] Z. Rafi, M. Umar Ijaz, A. Hamza, H. Ahmad Khan, Z. Ahmed, M. Nadeem Riaz, Protective effects of herbacetin against polystyrene microplastics-instigated liver damage in rats, J. King Saud Univ. Sci. 36 (2024) 103401.

[31] Y. Ge, S. Yang, T. Zhang, S. Gong, X. Wan, Y. Zhu, et al., Ferroptosis participated in inhaled polystyrene nanoplastics-induced liver injury and fibrosis, Sci. Total Environ. 916 (2024) 170342.

[32] H. Lin, X. Li, H. Gao, W. Hu, S. Yu, X. Li, et al., The role of gut microbiota in mediating increased toxicity of nano-sized polystyrene compared to micro-sized polystyrene in mice, Chemosphere 358 (2024) 142275.

[33] S. Mu, Y. Xu, Y. Zhang, X. Guo, J. Li, Y. Wang, et al., A non-peptide NIR fluorescent probe for detection of chymotrypsin and its imaging application, J. Mater. Chem. B 7 (2019) 2974–2980.

[34] Y. Zhao, X. Zou, X. Liang, L. Huang, W. Lin, A non-peptide chymotrypsin activatable probe for 3D-photoacoustic and NIR fluorogenic imaging of deep tumor, Sens. Actuators, B 382 (2023) 133553.

[35] S.-Y. Liu, X. Zou, X. Gao, Y.-Y. Zhang, De Novo Design of a Highly Selective Nonpeptide Fluorogenic Probe for Chymotrypsin Activity Sensing in a Living System, Anal. Chem. 94 (2022) 17922–17929.

[36] T. Lan, Q.-q. Tian, M.-h. Li, W. He, Activatable endoplasmic reticulum-targeted NIR fluorescent probe with a large stokes shift for detecting and imaging chymotrypsin, Analyst 147 (2022) 4098–4104.

[37] Y. Chen, J. Cao, X. Jiang, Z. Pan, N. Fu, A sensitive ratiometric fluorescence probe for chymotrypsin activity and inhibitor screening, Sens. Actuators, B 273 (2018) 204–210.

[38] J. Wang, Z. Teng, T. Cao, J. Qian, L. Zheng, Y. Cao, et al., Turn-on visible and ratiometric near-infrared fluorescent probes for distinction endogenous esterases and chymotrypsins in live cells, Sens. Actuators, B 306 (2020) 127567.

[39] C. Fan, J. Gao, Y. Gao, X. Yang, G. Li, X. Wang, et al., A non-peptide-based chymotrypsin-targeted long-wavelength emission fluorescent probe with large stokes shift and its application in bioimaging, Chin. Chem. Lett. 35 (2024) 109838.

[40] Y. Qu, Z. Xu, J. Wang, W. Liu, A. Iqbal, K. Iqbal, et al., Strong red fluorescent probe for detecting chymotrypsin activity in vivo and in vitro, Sens. Actuators, B 382 (2023) 133552.

[41] H. Xiong, R.-R. Li, S.-Y. Liu, F.-X. Wu, W.-C. Yang, G.-F. Yang, Discovery of specific nonpeptide probe for chymotrypsin via molecular docking-based virtual screening and the application, ACS Appl. Bio Mater. 1 (2018) 310–317.

[42] S. Saw, N. Arora, Protease inhibitor reduces airway response and underlying inflammation in cockroach allergen-induced murine model, Inflammation 38 (2014) 672–682.

[43] N. El Hadj Ali, N. Hmidet, N. Zouari-Fakhfakh, H. Ben Khaled, M. Nasri, Alkaline Chymotrypsin from Striped Seabream (Lithognathus mormyrus) Viscera: purification and characterization, J. Agric. Food Chem. 58 (2010) 9787–9792.

[44] A. Wallqvist, A.K. Smith, G.E.P. Ropella, M.R. McGill, P. Krishnan, L. Dutta, et al., Contrasting model mechanisms of alanine aminotransferase (ALT) release from damaged and necrotic hepatocytes as an example of general biomarker mechanisms, PLoS Comput. Biol. 16 (2020) e1007622.

[45] H. Ma, S. Chen, H. Xiong, M. Wang, W. Hang, X. Zhu, et al., Astaxanthin from Haematococcus pluvialis ameliorates the chemotherapeutic drug (doxorubicin) induced liver injury through the Keap1/Nrf2/HO-1 pathway in mice, Food Funct. 11 (2020) 4659–4671.